Shear testing and failure modelling of calcium phosphate coated AZ31 magnesium alloys for orthopaedic applications

Acheson, J. G., Gallagher, E. A., Ward, J., McKillop, S., FitzGibbon, B., Boyd, A., Meenan, BJ., Lemoine, P., & McGarry, J. P. (2022). Shear testing and failure modelling of calcium phosphate coated AZ31 magnesium alloys for orthopaedic applications. *Surface and Coatings Technology*, *429*, [127944]. https://doi.org/10.1016/j.surfcoat.2021.127944

Shear Testing and Failure Modelling of Calcium Phosphate Coated AZ31 Magnesium Alloys for Orthopaedic Applications

J.G. Acheson [a*`], E.A. Gallagher [b*], J. Ward [a*], S. McKillop [a], B. FitzGibbon [b, c], A.R. Boyd [a], B.J. Meenan [a†], P. Lemoine [a†], J.P. McGarry [b†`]

[a] Nanotechnology and Integrated Bioengineering Centre (NIBEC), School of Engineering, Ulster University, Shore Road, Newtownabbey, Co Antrim BT37 0QB, Northern Ireland, UK
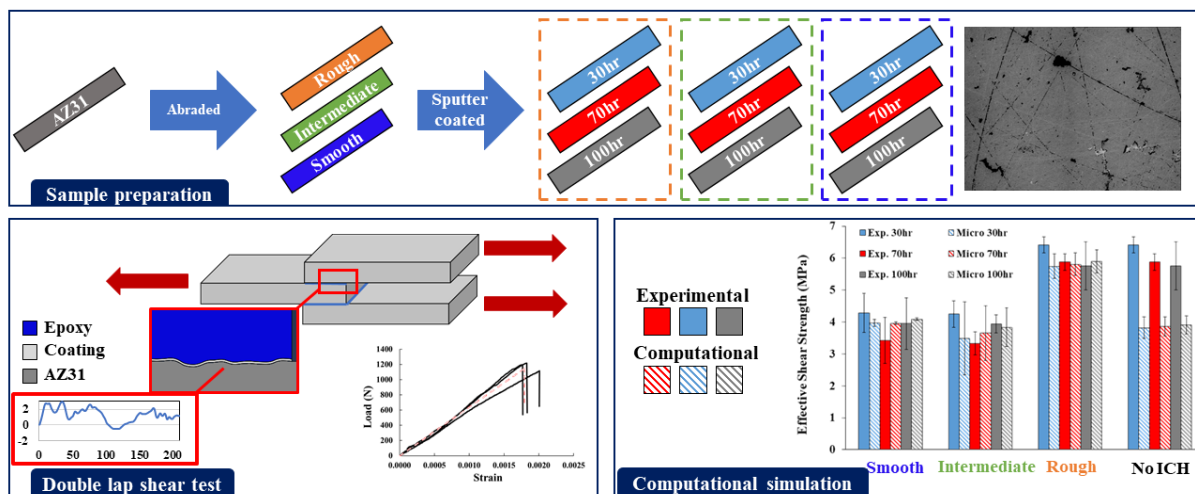[b] CÚRAM SFI Centre for Research in Medical Devices, Galway, Ireland
[c] Biomedical Engineering, College of Science and Engineering, National University of Ireland Galway, Ireland

[*]Joint first authors (j.acheson@ulster.ac.uk, +4428 9036 8663; patrick.mcgarry@nuigalway.ie, +353 9149 3165)
[†]Joint senior authors
[`]Joint corresponding authors

Graphical Abstract

Keywords: magnesium, calcium phosphate (CaP) coatings, double lap shear, finite element, cohesive zone

Abstract

Magnesium orthopaedic fracture fixation devices can potentially provide significant clinical benefits, such as the elimination of secondary surgeries for device removal due to *in-vivo* resorption and reduced stress shielding due to reduced device stiffness. However, development, approval, and clinical adoption of magnesium devices has been hindered by the excessively high rates of *in-vivo* corrosion such that the structural integrity of the device can be catastrophically reduced before fracture healing occurs. Coating of devices with calcium phosphate coatings has been shown to significantly reduce corrosion rates, while enhancing osseointegration. However, the adhesion strength between the CaP coatings and magnesium substrates has not been previously investigated. Clinical insertion of fracture fixation devices such as

1

intramedullary nails and k-wires will impose significant shear loading on the coated surface of the implant. If the effective shear strength of the coating-device interface is not sufficiently high, the coating will be damaged and removed during device insertion. In the current study a bespoke experimental-computational approach is developed to provide a new understanding of the relationship between coating thickness, surface roughness, and effective shear strength of the CaP coating- Mg substrate interface. Nine test cases were created by adjusting either the deposition time (3 thickness values) or the surface treatment of the Mg alloy using SiC paper (3 roughness values) and double-lap shear testing was performed for these coating configurations. Strain development in the Mg substrates was monitored using strain gauges, and failure stress was determined for each configuration. Test results revealed that the effective shear strength of the coating-substrate interface is significantly higher for coatings on the rougher substrate surfaces when compared to those on smoother surfaces. Coating thickness was not found to significantly influence the effective shear strength over the range considered in this study (0.37-1.34 µm). Micro-scale finite element models of lap-shear tests were constructed using experimental profilometry data. Simulations of rough coating-substrate interfaces reveal that significant localised compression occurs at the coating-substrate interface in regions of large asperities. A novel cohesive zone formulation has been developed to simulate compression induced shear hardening, and the resultant simulations are found to accurately predict the significantly higher effective shear strength measured experimentally for rougher coatings compared to smoother Mg substrate surfaces.

1   Introduction

Bone fractures are the leading cause of hospitalisations worldwide [1], with approximately 2.8 million bone repair cases performed annually [2]. The bone repair market was recorded at $53 billion globally in 2018, with the expectation of increasing to $75 billion by 2023 [3]. Commonly used biomaterials for this application include titanium, stainless steel and cobalt chromium, due to their strength and robustness that can substitute for hard tissue, such as bone. However, a major limitation with these materials exists within their inherently high elastic modulus which is not comparable to that for natural bone (3-20 GPa) [4]. This mismatch of mechanical properties leads to stress shielding whereby the typical stress on the bone is removed and causes bone resorption [5]. Metallic implants also provide a potential for ion release into surrounding tissues as a result of corrosion which may initiate an inflammatory response. Due to their non-degradability, there is generally a need for a second surgery to remove the device once the bone has healed. For example, titanium plates used for maxillofacial surgeries require removal in up to 40% of cases [6] due to plate migration, interference with subsequent imaging diagnostics, and sensitivity issues [7]. In the case of paediatric fracture fixation, post-healing surgical intervention can effect subsequent growth and remodelling of immature bone [8]. Hence, the creation of a biodegradable orthopaedic implant would eliminate the need for many of these removal surgeries, leading to reduced patient trauma and cost [9].

In this regard, magnesium and it alloys are attracting attention for use within orthopaedic applications due to their biocompatibility [10] and non-toxic biodegradability [11]. Stress-shielding is reduced by way of a lower elastic modulus (41-45 GPa) [12,13] and, due to the biodegradable nature of magnesium implants, second surgeries are becoming less prevalent [14]. However, despite research beginning back in 1878 [15,16] there still remains a core issue with magnesium in respect to its high degradation rate within the body [17,18]. Methods to control and tailor this degradation have been investigated by modification of the composition of magnesium alloys [19] and the application of coatings [20–22]. Alloying of magnesium with other elements such as calcium (Ca), aluminium (Al), and zinc (Zn) has been extensively investigated in recent years [23,24]. This process can increase both mechanical properties and corrosion resistance of

the magnesium alloy system. Surface treatment is another method which has been reported to control the rapid degradation of magnesium. Typical coating techniques within this category include electrochemical deposition, plasma spraying, chemical treatment, micro-arc oxidation and physical vapour deposition (PVD). Sputtering is the technique of choice for magnesium [25–27] due to the high adhesion strength and uniformity of the coating produced [28,29]. Other coating techniques possess limitations with non-uniformity on complex geometries [22,30], poor adherence [31] and cracking [32] which could potentially drive corrosion. Calcium phosphate (CaP) thin films sputtered using hydroxyapatite (HA) targets are among the most investigated sputter coating application for magnesium substrates [33–36]. Previous studies show that deposition of a CaP coating reduced corrosion rate in magnesium alloy coupons when subject to a degradation study using simulated body fluid (SBF) [21,37]. In general, coatings must be uniform and well adhered to facilitate adequate corrosion resistance [38].

Currently, there is a lack of literature surrounding the clinical study of CaP coated implants [39] and there are concerns surrounding the integrity of the coating post-implantation [40–43] with the high shear forces generated during implant insertion, having the potential to cause ploughing and/or delamination of the coating. Extensive research has been completed on CaP coatings and their role in slowing the degradation of the underlying substrate [21,44–46], however little is understood about its performance under mechanical stresses within clinical applications. Hence, in this study, the mechanical shear properties of CaP coatings on AZ31 Mg alloys have been investigated through an experimental double lap shear mechanical testing to determine the effects of coating thickness and AZ31 surface roughness on coating shear properties. The AZ31 Mg alloy has been selected due to its extensive research, commercial availability and cost effectiveness. These data have then been used to create a finite element (FE) model to simulate the failure of the CaP/AZ31 interface using a previously developed cohesive zone model (CZM) [47,48]. CZMs have been extensively used to predict interface failure and debonding of adhered surfaces [49–52] and to model the failure of polymer coatings on stents [52,53], as well as the delamination of plies in carbon fibre laminates [54,55] and the delamination of cells from substrates [56]. Specifically, both macro-scale and

micro-scale simulations of lap-shear experiments have been performed using experimental data from profilometer measurements in order to investigate the role of coating roughness and thickness on shear strength of the CaP/AZ31 interface.

2   Experimental Methods

2.1   Sample preparation

Commercial grade magnesium-aluminium-zinc alloy of nominal composition: 96% Mg, 3% Al, 1% Zn (AZ31, Goodfellow, UK) was used to create test substrates measuring 10 mm × 50 mm × 1 mm. Sets of substrates were manually abraded on all faces with SiC paper (RS-Components, UK) of varying grit size p240, p800 and p1200 to three distinct surface roughness conditions. Substrates were then placed in a beaker with 99% isopropanol (IPA) (Sigma Aldrich, UK) in an ultrasonic bath (Ultrawave Ltd., UK) for 5 minutes, before drying with lint free paper.

2.2   RF magnetron sputter coating

RF magnetron sputter targets were prepared by dry pressing 11.5 g of medical grade Captal "R" Hydroxyapatite (HA) (Plasma Biotal, UK) into a recessed copper disk using a stainless-steel die and compressing under a load of 80 kN for 60 seconds. RF magnetron sputtering was performed using a high vacuum physical deposition system configured with two Torus™ magnetron sputter sources (Kurt J. Lesker, USA) each of which is configured at an incident angle of 45° to the sample holder normal, as described in detail elsewhere [20,21]. Each source is operated at a frequency of 13.56 MHz with the main sputtering parameters used here detailed in

Table *1* to achieve coatings of various thickness, at a fixed throw distance of 100 mm, sputtering time was varied between 30, 70 and 100 hrs, with thicker coatings achieved after sputtering for a longer period of time. CaP coating thickness has been associated with sputtering parameters on a range of substrates with similar multielement targets [25,57–59]. More specifically, similar sputter targets have been used previously with the same conditions and yield a coating thickness which is comparable with this approach

[21,44]. Coatings were deposited on both faces of the substrate, across two sputter runs. Substrates were attached to the rotating sample holder via carbon tape and coated for the appropriate time. When finished, carbon tape was detached, and any residue removed using isopropyl alcohol before being thoroughly dried and coated on the remaining face.

Table 1 RF magnetron sputtering parameters.

Sputtering Parameter	Setting
Power	150 W
Ramp-up power	1 W/sec
Time	30/70/100 hrs
Chamber pressure	5×10^{-5} mbarr
Working gas	Argon (99.995%)
Gas flow rate	32 – 35 Sccm
Throw distance	100 mm

Coatings were sputter deposited, with no further processing and so are amorphous. In total, nine individual sets of samples were produced depending on the surface roughness and thickness conditions employed, as detailed in Table 2. Each sample set comprised three specimens with the required surface properties on both sides of the substrate(n=3).

Table 2 Table showing the nine sample types used.

		Coating thickness (hrs)		
		30hr	*70hr*	*100hr*
Surface roughness (grit size)	*p240*	n=3	n=3	n=3
	p800	n=3	n=3	n=3
	p1200	n=3	n=3	n=3

With regards to substrate surface roughness, samples are henceforth referred to as rough (p240), intermediate (p800) and smooth (p1200), where necessary.

6

2.3 Lap shear testing

Lap shear testing was performed by adapting the ASTM D3528 – 96 standard requirements for double lap shear testing of adhesive joints. CaP coated AZ31 samples (50 mm x 10 mm) of each type (Table 2) were then adhered to two uncoated AZ31 specimens, as shown in Figure 1, using a cyanoacrylate-based adhesive (Loctite Super Glue Power Flex Gel, Loctite, Germany). The mounted samples were then tested under tensile load using an Instron 2300 Mechanical Testing apparatus (Instron, USA) equipped with an axial extensometer; gauge length 25mm (model 3442; Epsilon Tech Corp, USA) at a crosshead speed of 1.27 mm/min, until failure.
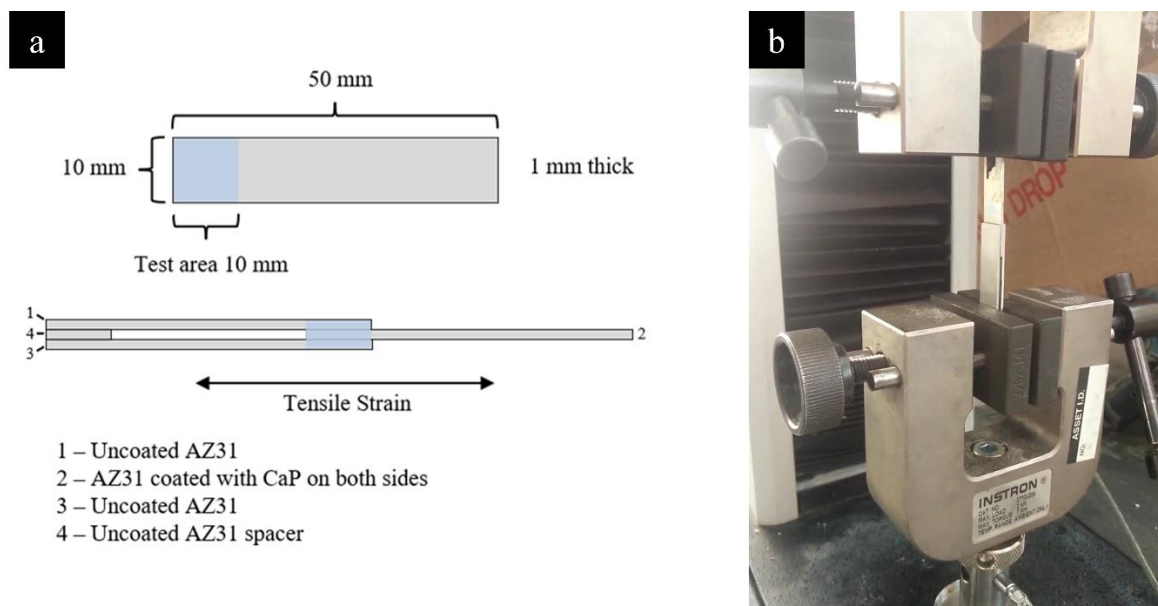

Figure 1 *(a) schematic detailing the construction of a double lap shear CaP coated AZ31 substrates and (b) illustration of how the double lap sample is incorporated within the tensile tester.*

2.4 Characterisation

The surface roughness of the uncoated, abraded (p240, p800, p1200 roughened) and CaP sputter coated (30, 70 and 100 hr) AZ31 substrates were measured using a DektakXT stylus profilometer (Bruker, UK), using a tip with diameter 2 µm, and force 2 mg. Data was measured across a distance of 4000µm, at a

resolution of 0.444 µm/pt. Roughness parameters Ra (mean surface roughness) and Rq (root mean square roughness) were recorded. Measurements were carried out in triplicate and t-tests were used to determine statistical difference (p value < 0.05). The results are presented as mean ± standard deviation, unless otherwise stated.

Time-of-Flight Secondary Ion Mass Spectrometry (ToF-SIMS) data was obtained using a ToF-SIMS 5 instrument (IONTOF GmbH, Germany). Analysis was carried out with a Bi^+ ion gun operating at 25 keV, in positive polarity, analysing an area of 20 x 20 µm. Depth profiling was performed with a secondary Cs^+ gun at 10 keV, rastered over an area of 100 x 100 µm. Data was collected using a non-interlaced sputtering technique for a sputter time of 1100 seconds. Data for Mg^+ and Ca^+ ions were recorded, with the cross over detection point used to determine coating thickness from a previously described equation [21]. This equation allows conversion of the ToF-SIMS depth profiling time to an exact thickness of RF magnetron sputtered CaP.

Scanning Electron Microscopy (SEM) with Energy Dispersive X-ray analysis (EDS) was carried out on post-lap shear substrates, using a Hitachi SU5000 field emission instrument (Hitachi, Europe) fitted with an X-max 80 silicon drift EDX analysis detector (Oxford Instruments, UK). SEM was carried out on the central beam of the double-lap shear specimen, with both sides being examined. High resolution images were captured in low vacuum, using the back-scattered electrons (BSE) signal. All images were collected under an accelerating voltage of 10 keV at a low magnification of ×60 to allow for a greater surface area (2 × 1.5 mm) to be analysed. High resolution images from four areas were then tiled together using the stitching plugin for ImageJ [60]. Grid collection stitching [61] was used to join images with a tile overlap of 6% and regression threshold of 0.10. EDX analysis was carried out under an accelerating voltage of 5kV in order to only analyse the coating, and not the underling magnesium alloy. EDX maps were recorded at a resolution of 1024 × 1024 pixels, with 3 frames acquired per map. These maps were used to create the chemical maps of the surface for use in conjunction with the grayscale SEM contrast images.

Further physical and chemical characterisation on said coatings has been completed in previous work published by the authors [21] and so, only relevant parameters were explored within this study.

3 Computational Methods

3.1 Cohesive Zone Model

To model the failure of the interface between the CaP coating and the Mg a non-potential based fully-coupled mixed-mode cohesive zone model is implemented (for full detail the reader is referred to FitzGibbon & McGarry [47]).

For a given interface displacement vector $\mathbf{\Delta}$ with normal and tangential (shear) components Δ_n and Δ_t, respectively, the corresponding displacement magnitude is given as $\Delta_m = \left(\Delta_n{}^2 + \Delta_t{}^2\right)^{1/2}$ and the mode angle is given as $\varphi = \tan^{-1}(\Delta_t/\Delta_n)$. The magnitude of the interface traction is expressed as a function of Δ_m and φ by the following formulation:

$$T_m(\Delta_m, \varphi) = \begin{cases} K_m\Delta_m \,, \Delta_m < \mathrm{T}_m^{max}(\varphi)/K_m \\ K_m\mathrm{T}_m^{max}(\varphi)/K_m\Psi(\varphi) \,, \Delta_m \geq \mathrm{T}_m^{max}(\varphi)/K_m \end{cases} \tag{1}$$

We refer to Ψ as the integrity of the interface (i.e., $\Psi = (1 - D)$, where D is referred to as the interface damage). Ψ monotonically decreases from 1 to 0 with increasing interface separation, such that

$$\Psi(\varphi) = \exp\left(-\frac{\Delta_m^{max} - \mathrm{T}_m^{max}(\varphi)/K_m}{\delta_m^*(\varphi)}\right)\frac{\Delta_m}{\Delta_m^{max}} \tag{2}$$

where K_m is the intrinsic elastic stiffness of the interface. K_m is assumed to be mode-independent. $\mathrm{T}_m^{max}(\varphi)$ is the specified mode-dependent interface strength; the corresponding displacement $(\delta_m^{el}(\varphi) = \mathrm{T}_m^{max}(\varphi)/K_m)$ represents the elastic limit of interface separation at the point of damage initiation. The mode-dependent parameter $\delta_m^*(\varphi)$ governs the rate of softening in the damage region ($\Delta_m \geq \mathrm{T}_m^{max}(\varphi)/K_m$). The interface strength is defined as a function of the mode as follows:

9

$$\mathrm{T}_m^{max}(\varphi) = \tau_{max} - \left(\frac{\tau_{max} - \sigma_{max}}{1 - \exp\left(-\frac{\frac{\pi}{2}}{\Omega^T}\right)} \right) \left(1 - \exp\left(-\frac{\varphi}{\Omega^T}\right)\right) \tag{3}$$

where τ_{max} is the mode II interface strength, Ω^T sets the non-linearity of the transition from mode II to mode I, and σ_{max} is the mode I interface strength. We specify the mode-dependence of $G_m(\varphi)$ using the following function:

$$G_m(\varphi) = G_t^0 - \left(\frac{G_t^0 - G_n^0}{1 - \exp\left(-\frac{\frac{\pi}{2}}{\Omega^G}\right)} \right) \left(1 - \exp\left(-\frac{\varphi}{\Omega^G}\right)\right) \tag{4}$$

where G_t^0 is the mode II fracture energy and G_n^0 is the mode I fracture energy, Ω^G sets the non-linearity of the transition from mode II to mode I. Finally, we complete the description of the cohesive zone formulation by decomposing T_m into the normal and tangential components, T_n and T_t, respectively, such that:

$$T_n = \begin{cases} K_{n_{oc}}\Delta_n, \Delta_n < 0 \\ T_m \sin(\varphi), \Delta_n \geq 0 \end{cases} \tag{5}$$

$$T_t = T_m \cos(\varphi) \tag{6}$$

where $K_{n_{oc}}$ is the overclosure penalty stiffness.

Finally, the model incorporates shear hardening due to normal compression at the interface. As shown in Figure 2, we include a dependence of the mode II interface strength, τ_{max}, on normal compression at the interface, such that

$$\tau_{max}(T_n) = \begin{cases} \tau_{max}^{nc}(T_n), \mathrm{T_n} < 0 \\ \tau_{max}^0 \quad , \mathrm{T_n} \geq 0 \end{cases}$$

The mode II interface strength increases with increasing (negative) normal traction, such that

$$\tau_{max}(T_n) = \begin{cases} \tau_{max}^0 + \tau_{max}^0(F_{oc} - 1.0)\left(1 - exp\left(\frac{T_n}{T_{oc}^*}\right)\right), T_n < 0 \\ \tau_{max}^0 \qquad , T_n \geq 0 \end{cases}$$

(7)

$$\tau_{max}^{nc}(T_n) = \tau_{max}^0 + \tau_{max}^0(F_{oc} - 1.0)\left(1 - exp\left(\frac{T_n}{T_{oc}^*}\right)\right)$$

where $\tau_{max}^{nc}(\Delta_n)$ is the increased value of tangential strength due to a normal compression at the interface. τ_{max}^0 is the maximum tangential strength, as encountered during a pure mode II separation when $\Delta_n = 0$ and $T_n = 0$. The parameter F_{oc} prescribes the maximum (plateau) value of increased shear strength due to compressive normal tractions at the interface. The parameter T_{oc}^* governs the sensitivity of maximum (plateau) shear stress to compressive normal tractions. Unless otherwise stated in this study, we assume that $\tau_{max} = \tau_{max}^0$, i.e. maximum tangential strength is not increased due to normal compression at the interface. This cohesive zone model is implemented in the finite element software Abaqus through a Used Defined Interface Subroutine (UINTER).
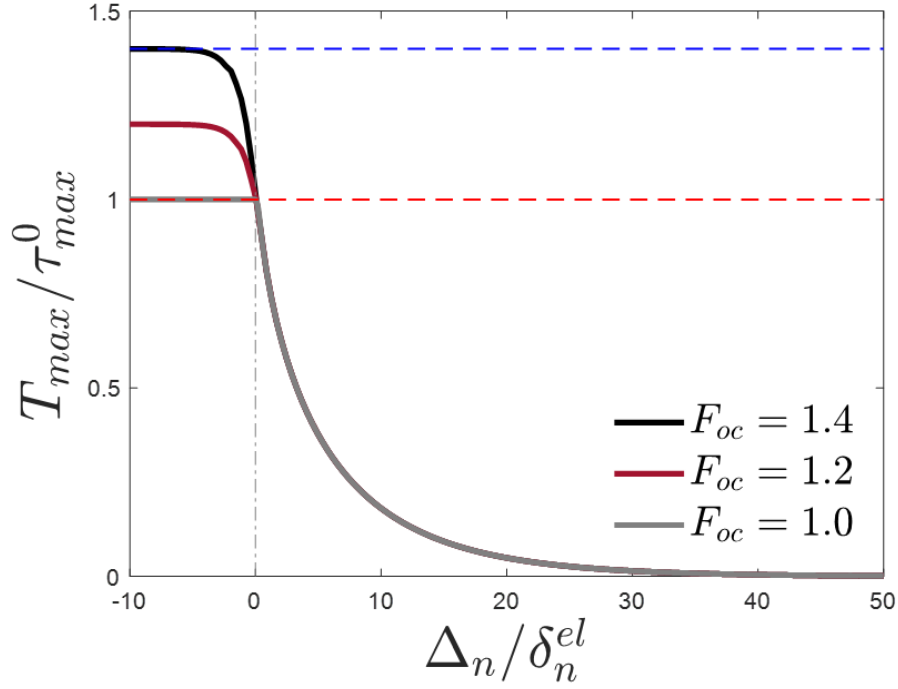
11

Figure 2 *Compression hardening law for three values of $F_{oc}=1.0, 1.2, 1.4$. The dashed red line indicates τ_{max}^0 and dashed blue line indicates the F_{oc} value used in the present study ($F_{oc}=1.4$). CZM parameters for this demonstrative example are $\tau_{max}=\sigma_{max}=1$ MPa, $G_t^0=G_n^0=1$ MPa/mm, $K_m=10$ MPa, $K_{n_{oc}}=K_m$, $T_{oc}^*=K_m/10$.*

3.2 Finite element model

As shown in Figure 3, a macro-scale finite element model of the experimental lap-shear experimental simulation is performed in which the CaP coating, the adhesive layer, and the CaP/Mg interface is phenomenologically represented using the cohesive zone formulation (equations (1)-(8)). The CZM elastic stiffness is calibrated to account for the elastic deformation of the coating, and the CZM effective shear strength is calibrated based on experimental measurements of applied force at the point of interface failure. In such macro-scale simulations, the interface is assumed to be planar, and mixed-mode interface separation does not occur. Therefore, the macro-model determines the mode II interface strength (τ_{max}), the mode II fracture energy (G_t^0) and the effective stiffness (K_m) of the interface at a continuum level.

These parameters are determined individually through separate sensitivity analyses of each parameter fitting computational reaction force to experimental reaction force.

This mode II interface strength is a function of both the chemical bond strength between the CaP and the Mg as well as the geometric conditions (i.e., the surface roughness of the Mg) which are not explicitly modelled in the macro-scale simulation.

Additionally, micro-scale simulations are also performed in which a realistic coating geometry is explicitly constructed using experimental thickness measurements and experimental profilometry characterisation of the surface roughness. The adhesive layer is also explicitly represented in the model. The CZM formulation is applied to the rough surface interface between the CaP coating and the Mg. In such micro-scale modelling the CZM represents only the chemical bonds between the CaP and Mg, with CZM parameters representing the bond strength, and fracture energy. Additionally, due to the complex geometry of the CaP-Mg interface, mixed-mode debonding can occur, despite the effective application of a pure shear deformation at the macro-scale. Additionally, the complex interface geometry can result in compression between contacting asperities during the fracture process, which can also provide a toughening mechanism against crack propagation and interface failure. Micro-scale model material properties used are outlined in Table 3.

Table 3 *Material properties used in the FE models.*

Material	E, Young's Modulus (GPa)	Poisson's Ratio
Magnesium [19]	45	0.35
CaP coating [62]	130	0.4
Adhesive [63]	1.7	0.4

Individual micro-models are created for each of the 9 experimental test cases outlined in section 2.1. A Python script is developed to construct the CaP-Mg interface surfaces. Experimentally measured topographical data from the experimental profilometry data sets for each roughness value. Two micro-scale surfaces along with their corresponding topographical data for the roughest and smoothest surfaces are displayed in Figure 3. Furthermore, from each of the 3 sets of experimental profilometer data, three statistically similar but topologically different Mg surfaces are created, ensuring that roughness of each

13

section is within 5% of the experimentally measured roughness value. This ensures that the predicted micro-scale results are not due to a geometric anomaly. Three values of coating thickness are considered for each reconstructed CaP-Mg interface. A total of 27 micro-scale models are simulated. The CaP-Mg interface strength and fracture energy are calibrated so that the resultant stress and displacement at interface failure is the same as the effective values determined by the aforementioned experiments and macro-scale simulations. This micro-scale modelling approach is used to determine if measured experimental trends of can be predicted solely from the changes in surface roughness or coating thickness, i.e., if the same chemical bond exists between the CaP coating and the Mg for all experiments.
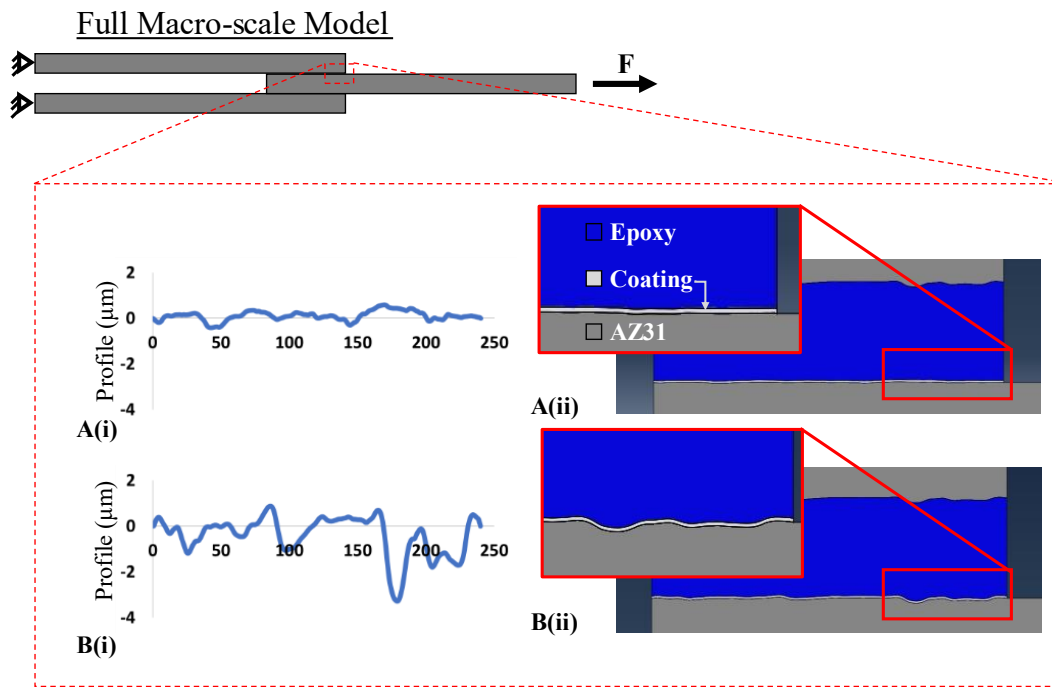

Figure 3 *Schematic of the full macro-model with an overlap length of 10 mm matching the experimental tests. The detail view shows the experimentally measured topographic data for a section of one A(i) p1200 surface and one B(i) p240 surface. Images of the corresponding surfaces in the micro-scale models for the A(ii) p1200 surface and the B(ii) p240 surface, where zoom boxes are show for more detail of the coating thickness (cream) compared to the adhesive (blue) and the Mg (grey).*

All computational simulations are carried out in the commercial FE software Abaqus 2017 (Dassault Systems). The macro-model is comprised of 9600 CPE4 elements. In order to account for machine compliance that is evident in the experimental results a spring-to-ground is included at the fixed end of the

14

sample with a spring stiffness of 140 kN/m, which gave a good fit with the experimental results. The micro-

scale finite element models are comprised of approximately 700,000 CPE3 and CPE4 elements.

4   Experimental Results

Substrates abraded with SiC paper of p240, p800 and p1200 grit size yield mean surface roughness values

of 0.87 ± 0.13, 0.27 ± 0.04 and 0.16 ± 0.04 µm, respectively, as shown in Figure 4. All substrates are found

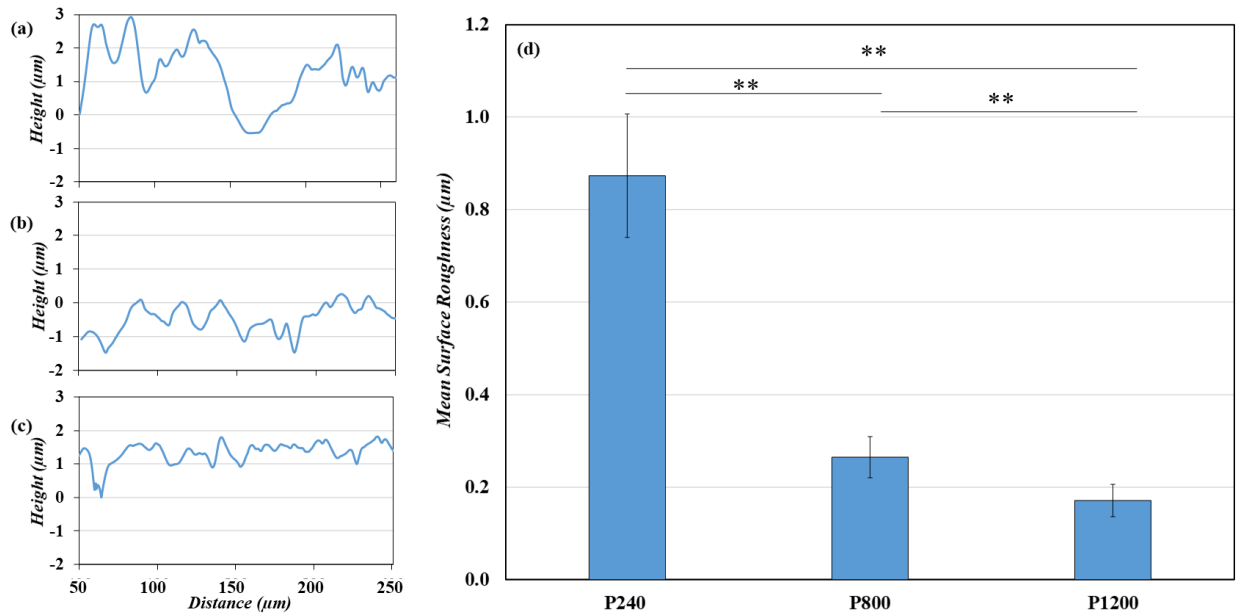to have surface roughnesses that are significantly different (p<0.01) from one another.

Figure 4 *Stylus profilometer line profiles of substrates abraded with (a) p240, (b) p800 and (c) p1200 grit paper with (d) comparison of mean surface roughness (Ra).   **Statistical difference: p240/p800 (p<0.01); p240/p1200 (p<0.01); p800/p1200 (p<0.01).*

Figure 5 shows the Time-of-Flight Secondary Ion Mass Spectrometry (ToF-SIMS) depth profiles for a p240

specimen from each sputter run, plotting sputter time versus intensity. Coating thickness is measured as

0.37, 0.83 and 1.34 µm corresponding to a RF sputtering time of 30, 70 and 100hr.
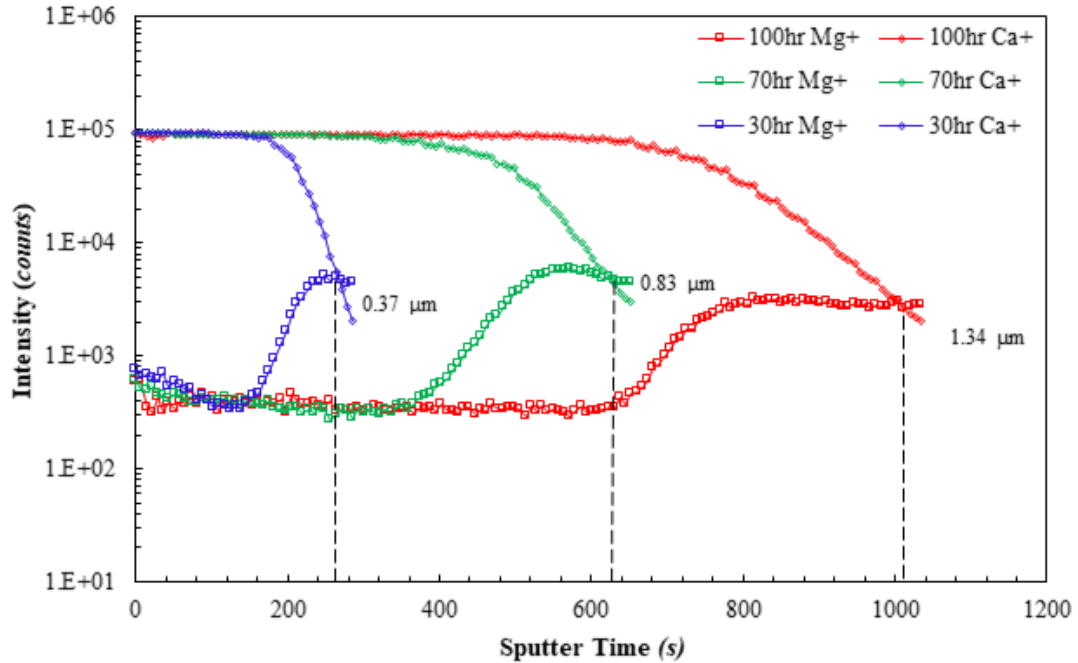
Figure 5 *Depth profile analysis of 30 (blue), 70 (green) and 100hr (red) RF magnetron sputtered CaP coatings on p240 AZ31 magnesium alloy. Coating thicknesses were calculated using a sputter rate ratio obtained from analysis of a Ca+ depth profile crater using the same settings under stylus profilometry, as described previously* [21].

Table 4 shows the results from the double lap shear mechanical testing with the load to failure reported as a mean (n=3) ± standard deviation. Results here indicate that as surface roughness increases, a larger load to failure is required. Statistical comparison shows that with respect to surface roughness, load to failure for p240 samples is significantly higher than for the p800 and p1200 surfaces (p<0.01). No significant difference is present between failure loads for p800 and p1200 substrates. Hence, coating thickness does not show a significant difference with respect to load to failure.

Table 4 *Influence of coating thickness and surface roughness on experimental effective shear strength (MPa) required to cause failure.*

		Coating thickness (Deposition time)		
		0.37 µm (30hr)	*0.83 µm (70hr)*	*1.34 µm (100hr)*
Surface Roughness (grit)	*0.87 µm (p240)*	6.42 ± 0.25	5.88 ± 0.27	5.75 ± 0.75
	0.27 µm (p800)	4.25 ± 0.41	3.33 ± 0.36	3.94 ± 0.28
	0.16 µm (p1200)	4.28 ± 0.61	3.42 ± 0.72	3.95 ± 0.81

Scanning electron microscopy analysis of a p240 polished, 70hr CaP coated substrate, post lap-shear is shown in Figure 6 with EDS elemental maps for the magnesium, calcium and phosphorus signals together with an overlaid image also provided. For the central beam of the double-lap specimen, the CaP coating remains mostly within the striations, with the majority being removed by the shear forces applied during testing.
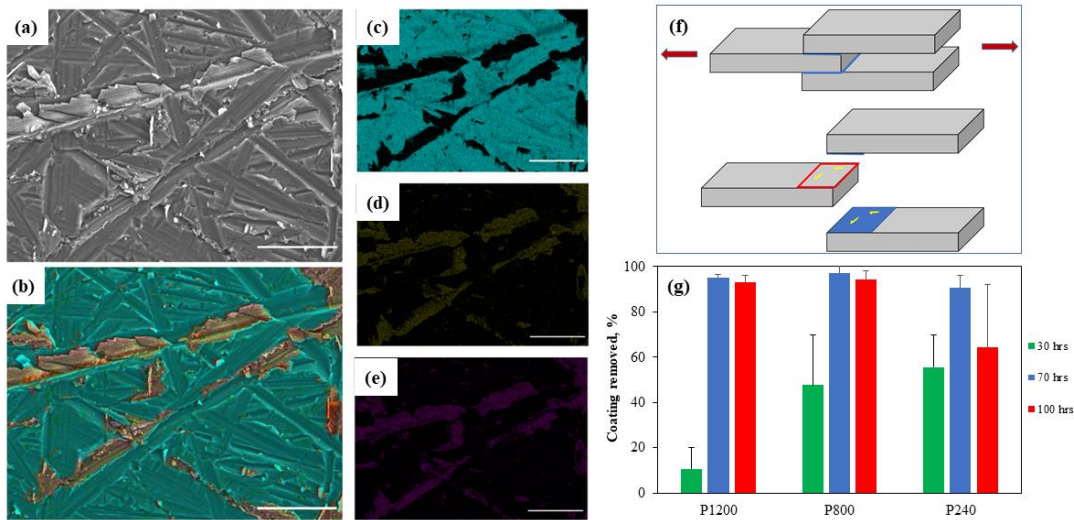

Figure 6 *SEM/EDX analysis of failed double-lap central beams for CaP coatings deposited for 70 hr AZ31 Mg alloy substrates; polished with p240 SiC paper. (a) SEM high resolution image, (b) EDX elemental composition overlay, (c) magnesium, (d) calcium and (e) phosphorus elemental maps. Scale bar = 50 µm. The schematic in (f) shows the central beam's surface analysed (red contoured) and the bar chart in (g) displays the removed CaP coverage, based on similar EDS maps, for different AZ31 roughnesses and CaP thicknesses.*

Indeed, quantitative analysis of the amount of coating removed after shear to failure was carried out to determine if there was any relationship between load to failure and the proportion of coating removed from a standard 4×3 mm^2 area. This was done using grayscale thresholding and pixel counting, with results displayed in the bar chart of Figure 6 (g). These data indicate that the coating removal fraction tended to decrease for the rougher and thicker coatings, except in the case of 30hr substrates.

Data from EDX analysis of these coatings is presented as Ca/P ratios which have been calculated based on percentage atomic concentration (Table 5).

Table 5 *Ca/P ratios determined by SEM-EDX analysis for different CaP coating thickness parameters on AZ31 Mg alloy.*

Substrate	Ca/P ratio
0.37 μm (30hr)	1.51 ± 0.04
0.83 μm (70hr)	1.79 ± 0.09
1.34 μm (100 hr)	1.84 ± 0.09

5   Computational Results

5.1   CZM Parameter calibration

In order to estimate the Mode II interface strength, fracture energy, and effective stiffness a sensitivity analysis is carried out for each cohesive zone parameter (Figure 7). The output from such parametric simulations is a macro-scale lap-shear force-displacement curve that can be compared directly to experimental measurables. Simulations reveal that the cohesive zone mode II strength (τ_{max}) primarily influences the peak lap-shear force, and consequently the effective shear strength. The cohesive zone mode II fracture energy primarily determines the rate of force reduction after the peak force is reached. The cohesive zone intrinsic elastic stiffness primarily influences the slope of the lap-shear force displacement curve prior to the peak force. These dependencies allowed for an accurate calibration of the cohesive zone mode II fracture strength from experimental results. In the case of the cohesive zone fracture energy G,

experimental measurements allowed for the establishment of an upper limit that accurately simulated the brittle fracture observed in lap-shear tests.

Figure 7(A) presents a parametric study of the mode II interface shear strength (τ_{max}) using a fracture energy, G, and the interface stiffness, K_m, of 0.18 MPa/mm and 200 MPa, respectively, for all cases. The interface strength has a significant effect on the applied force at failure. As expected, the effective stiffness is not influenced by this parameter.

Next, the effect of the interface stiffness, K_m on predicted force vs strain curves is presented in Figure 7(B). In all cases the mode II interface strength, τ_{max}, and the fracture energy, G, have values of 4.8MPa and 0.18 MPa/mm, respectively. The CZM effective stiffness K_m has a significant effect on the predicted stiffness of the system, while having a weak (but non-negligible) effect on the applied force at failure.
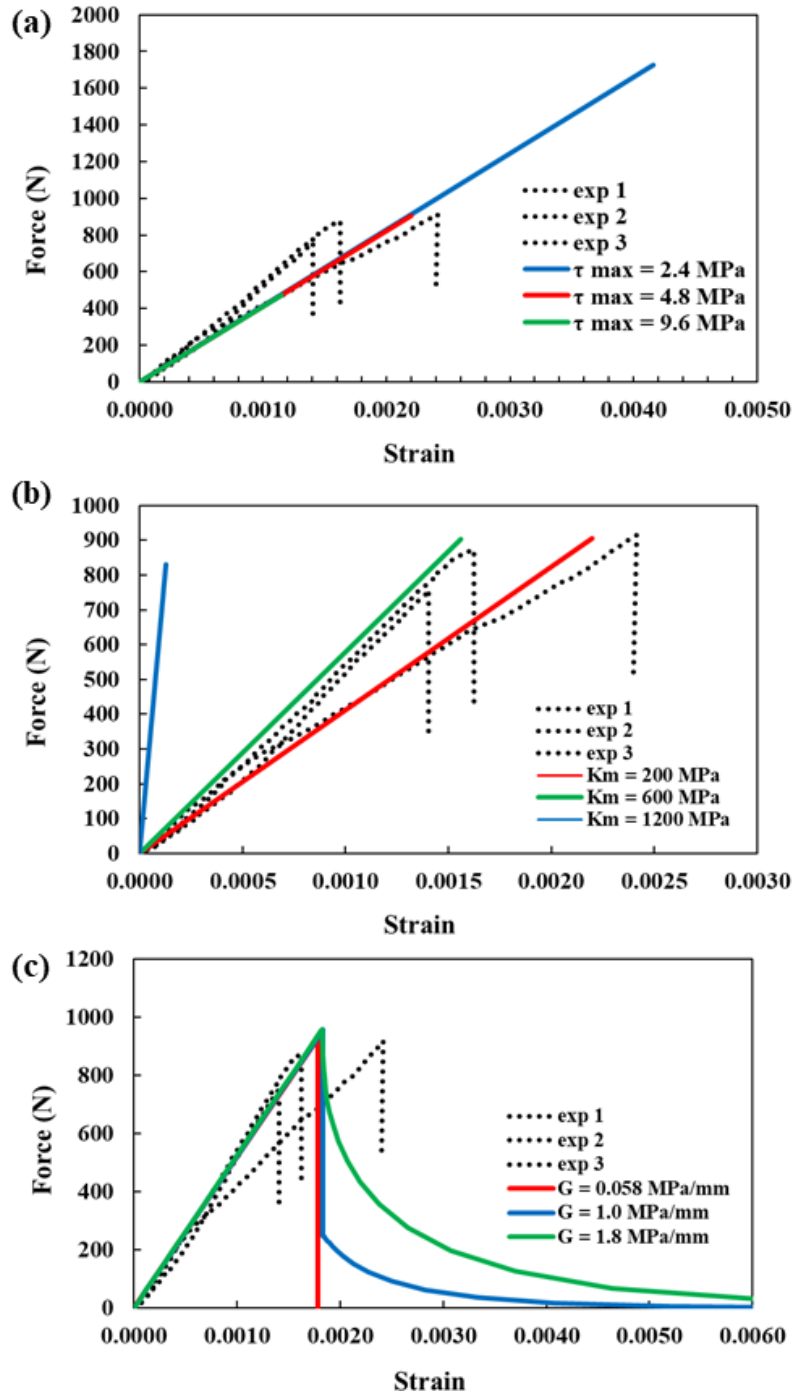
Figure 7 *(a) A graph of force (F) versus strain (measured at the extensometer) plotting the experimental results and the computational results for different interface strength values. (b) A graph of force (F) versus strain (measured at the extensometer) plotting the experimental results and the computational results for different interface stiffness values. (c) A graph of force (F) versus strain (measured at the extensometer) plotting the experimental results and the computational results for different fracture energy values. All experimental samples had roughness of Ra=0.27 µm and thickness of 0.37µm.*

Finally, we examined the effect of the CZM fracture energy (G) on the system. For the results plotted in Figure 7(C), the interface strength (τ_{max}) and the interface stiffness (K_m) have values of 4.8MPa and 200MPa, respectively. The fracture energy has a negligible effect on the applied force at failure, but it has a strong influence on the softening behaviour following initiation of crack propagation. Experimentally a sudden drop in applied force is observed, with fast crack propagation through the interface. This suggests that brittle interface fracture occurs with a low interface fracture energy. As shown in Figure 7(C), a fracture energy (G) of 1.0 MPa/mm provides a reasonable upper limit for prediction of experimentally observed brittle interface failure. Higher values of fracture energy result in a more gradual reduction in force following initiation, in contrast to experimentally observed rapid reductions in force. Further reduction of G below 1.0 MPa/mm does not significantly influence the predicted peak force or the subsequent rapid reduction of force during brittle fracture.
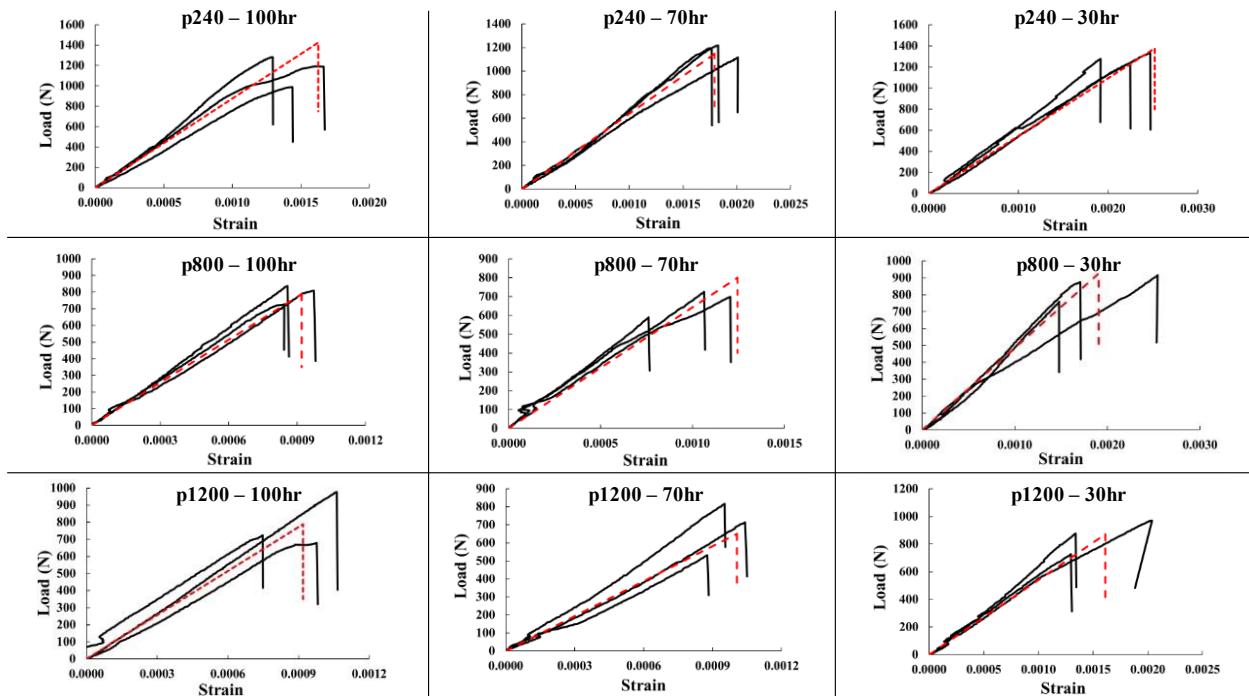

Figure 8 *Load vs displacement graphs for each of the 9 cases tested. The experimental results are shown in black, and the computational fits are shown in a dashed red line.*

Computational and experimental load-displacement curves are superimposed in Figure 8 for each of the nine experimental coating configurations. As shown in Figure 8, the model accurately predicts the linear load-strain relationship, in addition to the failure load and failure strain for all cases. The calibrated CZM shear strengths (τ_{max}) are similar in value to the experimentally measured effective shear strength. This indicates that, at a macro-scale, interface failure during a lap-shear test can be represented as a pure mode II process. Similar to experimental trends, the computational CZM interface strength is found to be strongly dependent on coating roughness, but not on coating thickness. CZM stiffness is calibrated to accurately predict the pre-failure slope of experimental force-strain curves. energy of 1.0 MPa/mm is found to predict sufficiently fast crack growth and brittle fracture (similar to that observed experimentally) for all nine coating configurations.

Table 6 *Calibrated τ_{max} (MPa) parameters for the CaP/Mg interface in the macro-scale lap-shear model*

		Coating thickness (Deposition time)		
		0.37 μm (30hr)	*0.83 μm (70hr)*	*1.34 μm (100hr)*
Surface Roughness (grit)	*0.87 μm (p240)*	7.3	6.0	9.0
	0.27 μm (p800)	4.8	4.1	4.1
	0.16 μm (p1200)	4.5	3.3	4.1

5.2 Micro-scale Computational Analysis

Incorporation of experimentally measured coating roughness profiles into micro-scale finite element models of lap-shear tests provides insight into the role of localised compression hardening and crack-tip mode mixity on the effective shear strength of the coating-substrate interface. Figure 9 presents the stress state in the coating and the traction state at the coating-magnesium interface at the point of fracture initiation. For both the rough and smooth coating profile, crack initiation is a mixed mode process, with significant normal separation, in addition to tangential/shear separation. As a result, the local micro-scale mode I and mode II strengths (σ_{max}=13 MPa; τ_{max}=13 MPa) are found to be significantly higher than the

22

calibrated values for the macro-scale model (Table 6) due to its simplified assumption of a perfectly planar interface and pure mode II debonding throughout the lap-shear failure.
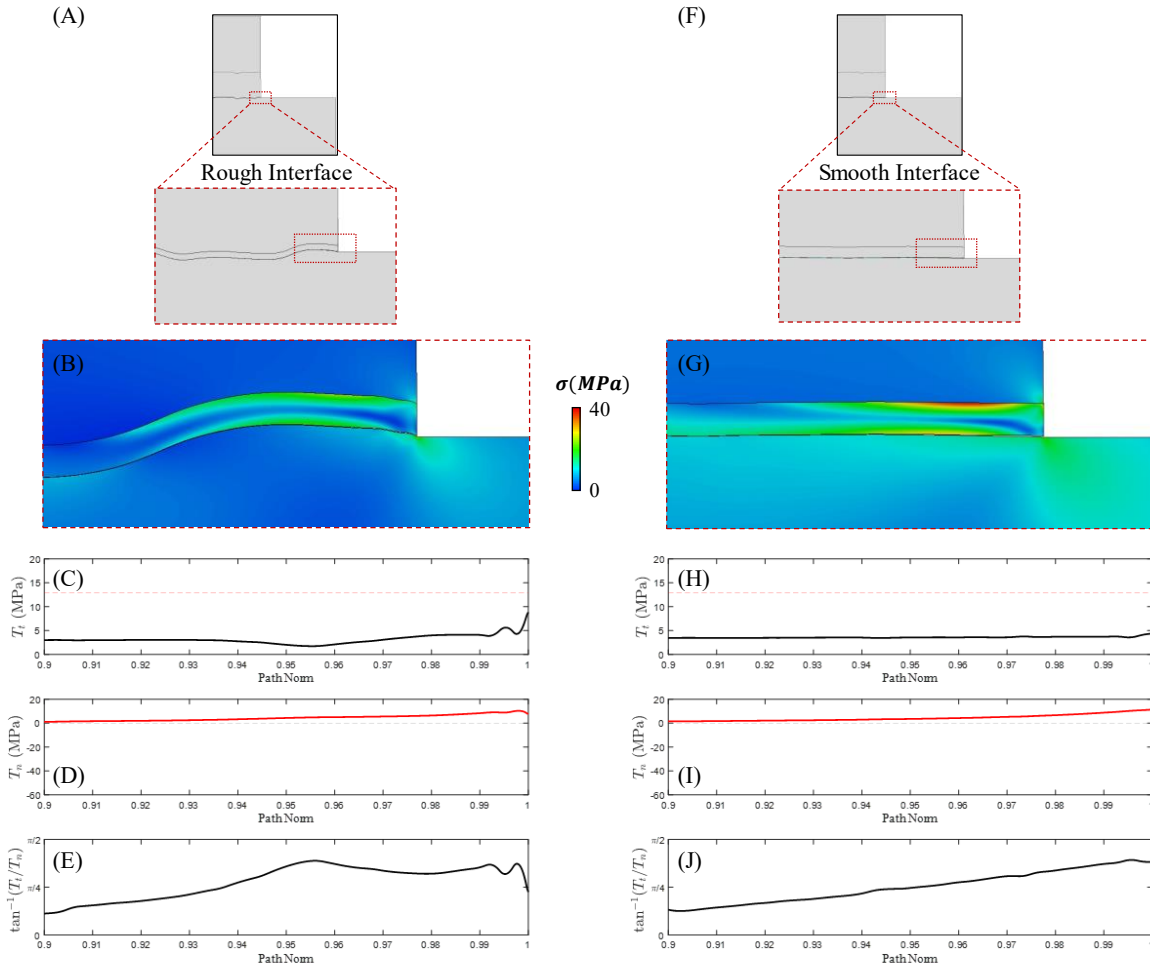

Figure 9. *Stress state and traction state in the coating at the point of initiation in the rough model (A-E) and the smooth model (F-J). Computed Von Mises stress in the rough model (B) and the smooth model (G) is shown. Tangential traction (C, H) and normal traction (D, I) are shown for the selected potion of the interface. The traction-based mode mixity* $\tan^{-1}(T_t/T_n)$ *is shown in (E, J), mixed mode initiation is evident in the smooth and rough models.*

Figure 10 shows the stress state and the interface traction state as a crack grows from a non-compressive region (at the base of a large asperity on a rough coating) towards a region of high interface compression at the side of the asperity. Prior to the crack-tip entering a compressive zone, crack extension occurs when the pure mode II interface shear strength is reached. However, as the magnitude of interface compression

23

increases at the crack tip, the mode II interface strength is increased due to an interface compression hardening (ICH) mechanism, as described by equation (9), with parameters $F_{oc} = 1.4$ and $T_{oc}^* = K_m/100$.
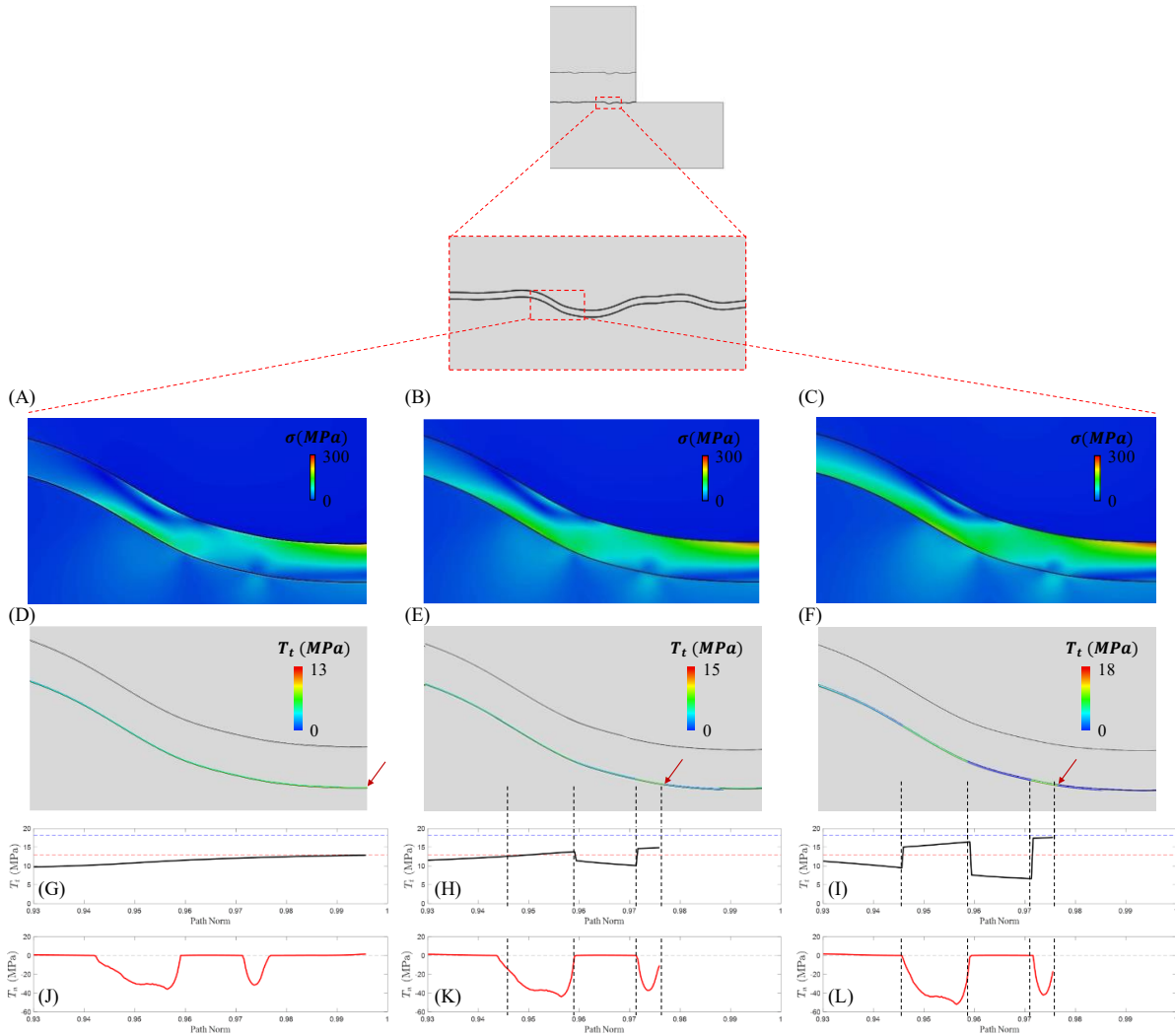

Figure 10 *Micro-scale ICH model prediction of crack propagation along a large asperity in a rough coating. Von Mises Stress distributions in coating and substrate are shown in (A-C). Tangential traction (T_t) distributions along the asperity during crack propagation are shown in (D-F). Tangential traction (T_t) (G-I) and normal traction (T_n) (J-L) are plotted as a function of position in front of the crack tip. In regions of high interface compression (negative normal traction) on the side of the asperity, the shear strength is significantly increased due to an interface compression hardening mechanism.*

In the case of a smooth coating, as shown in Figure 11, the absence of such regions of interface compression due to significantly lower roughness and asperities results in negligible compression hardening.
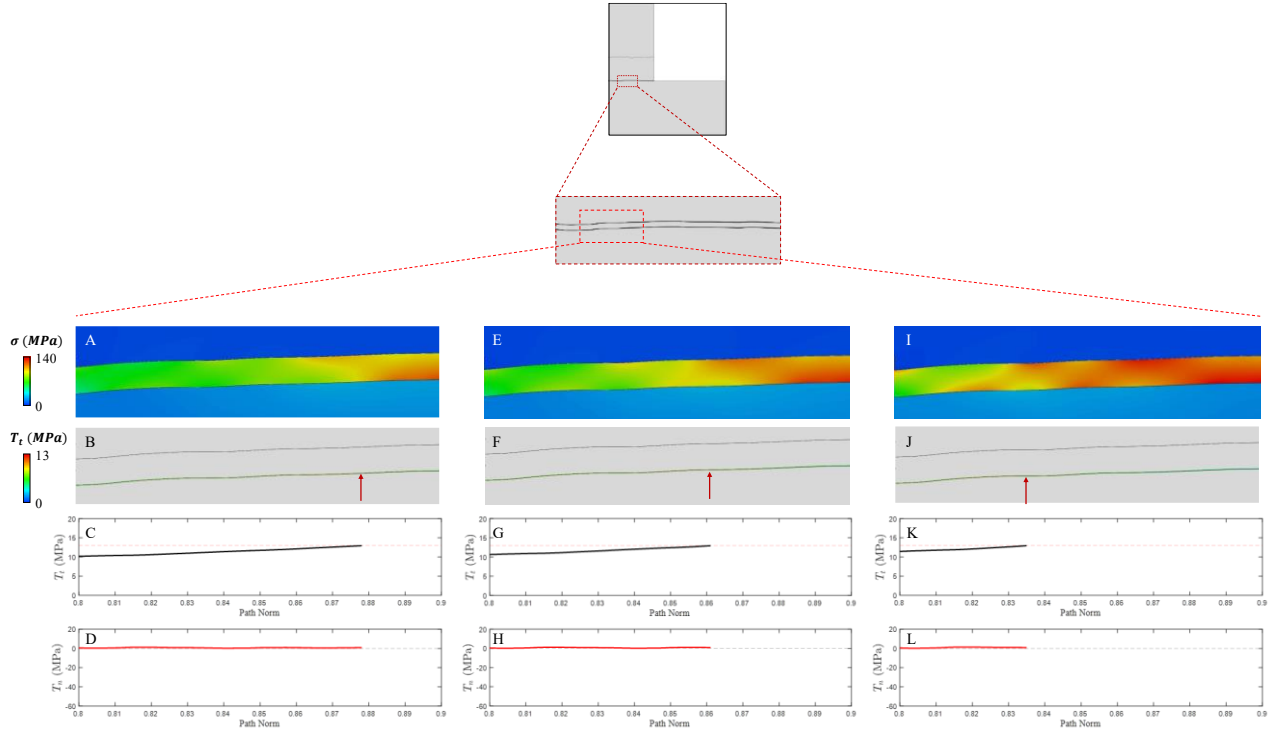

Figure 11 Micro-scale ICH model prediction of crack propagating along the smooth coating. Von Mises stress in the smooth coating is computed (A, E, I). Tangential traction (B, C, F, G, J, K) and normal traction (D, H, L) along the interface of the smooth coating. In contrast to a rough coating, no regions of high compression are computed along the interface, and consequently no significant compression hardening is computed. The red arrow denotes the position of the crack tip.

Consequently, as shown in Figure 12, the effective shear strength of the rough coating is computed to be ~1.75 times higher than that of a smooth coating, in agreement with experimental measurements. Micro-scale profilometer based models predict that effective shear strength is independent of coating thickness for a given roughness level. The ICH mechanism is not found to depend on coating thickness. This computed result is also consistent with experimental results and suggests that interface compression at asperities and related shear hardening is the primary determinant of effective shear strength. If the ICH mechanism is removed from the model, the experimentally observed higher effective shear strength is not computed for the rough coating. Finally, effective shear strengths are computed for five representative, experimentally

25

measured coating profiles for each case. This facilitates the computation of a mean and standard deviation of computed effective shear strength for each case. No statistically significant differences are observed between computed and measured results when the ICH mechanism is incorporated into the micro-scale modelling framework.
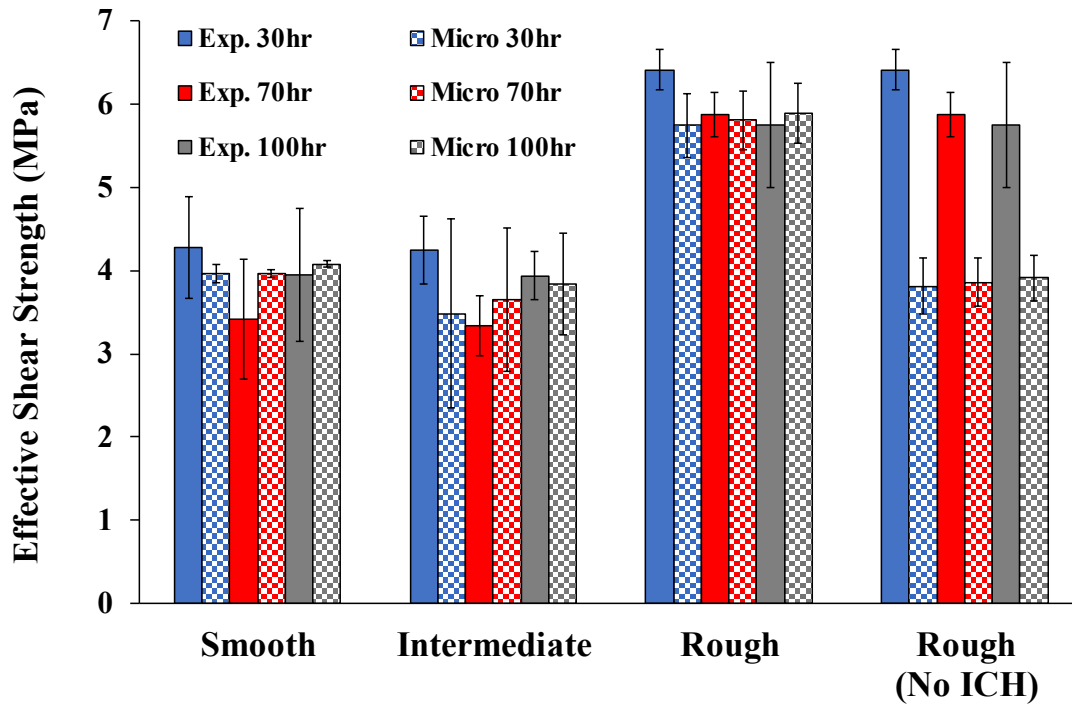

Figure 12 *Computed values of effective interface mode II strength for smooth, intermediate, and rough coating-substrate interfaces. Computed results are presented as mean and standard deviations using five representative, experimentally measured profilometer date for each case. Incorporation of the ICHM results in a significant increase in effective mode II strength for rough coating-substrate interfaces, providing good agreement with experimental measurements.*

While micro-scale simulations suggest that large asperities in rough coatings result in compressive interface stresses which result in interface shear hardening and higher effective shear strength, an addition consequence of such localisation is the generation of higher stresses within the coating itself. Figure 13 the stress state in the coating ahead of the crack tip is analysed in detail for a rough and smooth coating. Clearly, the presence of large asperities results in shear stress localisations as high as 157 MPa in the rough coating

26

(Figure 13A), whereas shear stresses of 73 MPa are only computed in the smooth coating (Figure 13B). A similar trend of localisations of the maximum principal (tensile) stress is computed in the rough coating (69 MPa, Figure 13C) compared to the smooth coating (2 MPa, Figure 13D). Finally, such localisations are also computed in the minimum principal (compressive) stress in the rough coating (309 MPa, Figure 13E) compared to the smooth coating (147 MPa, Figure 13F). While the computed minimum principal stress localisation is not sufficient to cause failure with a compressive strength of 510 MPa [64], it could conceivably reach this value in specimens with more severe asperities (rougher interfaces). While precise values of shear strength have not been determined for CaP coatings, localisations in excess of 150 MPa are in the region of reported tensile strength for dense calcium phosphate materials (69-193 MPa) [64]. Furthermore, the computed max principal stress localisation is at lower end of this range (69 MPa) suggesting it may also play a role in coating failure. Such localisations persist in the coating following localised debonding at the interface due to hard contact between coating and substrate in the region of the asperity. In summary, an increase in coating roughness may increase the resistance to interface debonding due to localised interface compression. However, such an increase in roughness will also elevate localised stresses in the coating material, thus activating intra-coating damage as a secondary mechanism of failure. This may provide an explanation for the experimental observation that ~10% of the coating remains on the substrate following lap-shear testing (i.e., localised sections of damaged coating may remain in place) and the decreased removed coverage fraction of Figure 6 (g). Such high stress localisations in the coating material are not computed in the smooth coating. This prediction is consistent with the experimental observation that only ~3% of a smooth coating remains on the substrate following lap-shear testing.
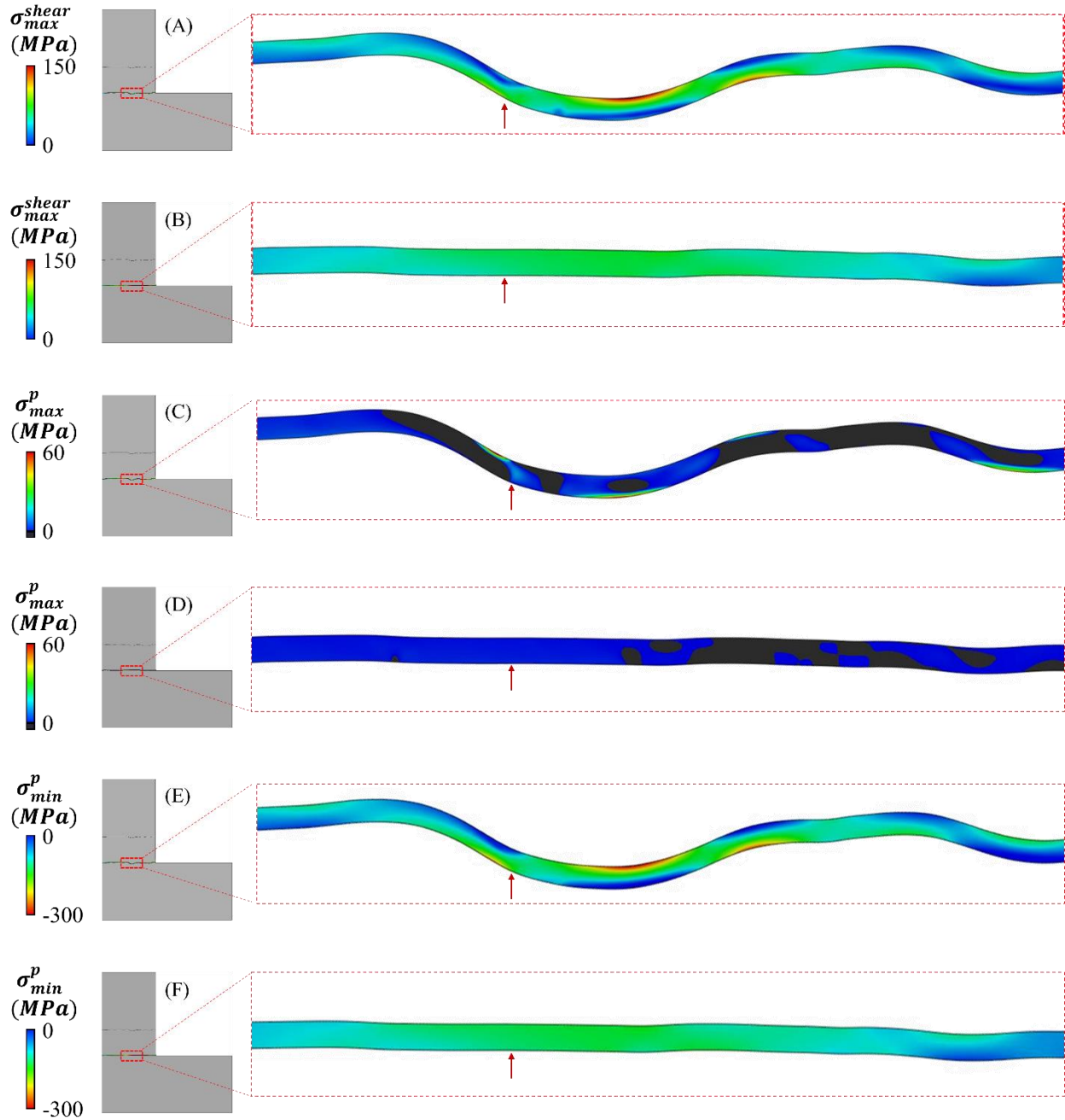
Figure 13. *Max shear stress in the coating for the rough (A) and smooth (B) interfaces. The red arrow denotes the location of the crack tip 68.4 μm from the edge of the sample. The max tensile (principal) stress is shown in (C) and (D) for the rough and smooth interfaces, respectively. Minimum principal stress is shown in (E) and (F) for the rough and smooth interfaces, respectively. The red arrow denotes the location of the crack tip 68.4 μm from the edge of the sample in each case.*

6   Discussion

EDX analysis of CaP coatings Mg alloy substrates pre-lap shear testing, indicate Ca/P ratios of 1.51, 1.79 and 1.84 for thicknesses of 0.37, 0.83 and 1.34 µm, respectively. These values are slightly lower than that of stoichiometric hydroxyapatite (1.67). Though, they are comparable to previously reported work with RF sputter-deposited amorphous CaP coatings on both standard metal and metal alloy substrates [44,57,65]. It is thought that the abrasive preparation of the Mg substrates effects the growth mechanism of the coating which in turn can contribute to a lower Ca/P ratio [39].

The results presented here indicate that as surface roughness increases, so too does the shear strength of the CaP sputter-deposited coating on the Mg alloy. Previous studies report that an increased surface roughness acts to increase the mechanical interlocking effect between the adhesive and sample surface [66,67]. With regard to the coating thickness, there is no clear relationship between thickness and effective shear strength. In this study, it is clear that substrate roughness impacts on the shear strength of this CaP coating - magnesium alloy substrate interface to a greater extent than coating thickness.

Due to the complex loading environment experienced by orthopaedic fracture fixation devices such as K-wires and intra-medullary nails, particularly the extremely high shear loads on insertion, it is essential that the CaP coating applied to Mg implants remains intact post-surgery. Any defects or failures that occur in the coating during insertion could potentially represent areas for stress localisations and increased degradation rates for the Mg implant. As such, it is essential that the nature interface between the CaP coating and the Mg alloy is optimised for these conditions. The CZM data presented in this study has been calibrated to accurately predict the strain and load at failure observed in the experimental portion of this paper.

Currently no recommendations or regulatory guidelines are in place for lower limits of shear strength at implant-coating interfaces and the required coating strength for use *in vivo* will be highly application-specific. However, previous finite element analyses of intramedullary nails and fracture fixation locking plates suggests interface shear stresses are lower than ~10 MPa [68]. In said analyses the majority of the

29

surface area of an intramedullary nail, subjected to physiologically relevant loading conditions, does not exceed the effective shear strength of ≈6.5 MPa uncovered in the present study. Only one of the reinforcing screws is found to exceed the magnesium-HA effective shear strength. Therefore, we suggest that the magnesium-HA system fabricated in the current study could be a viable candidate for intramedullary nails applications. However, further detailed finite element analysis should be carried out in order to determine application-specific required coating strengths. This could lead to the modification of implant designs in order to reduce shear-stress at the coating-implant surface.

Macro-scale CZM parameters as calibrated herein are a good fit for the experimental results achieved. Macro-scale model does not explicitly model the surface roughness and coating thickness due to computational restrictions. The highest macro-scale interfacial strength is predicted for the samples with the roughest surface, Ra= 0.87 µm, with little difference in the values predicted for the two smoother surfaces. Results show no statistical significance in the macro-scale interface strength for the three coating thicknesses studied and do not clarify what effect, if any, topography and the coating thickness specifically have on the interface strength and so a micro-scale model was developed to provide further insight.

The micro-scale model presented in the current study accounts for the mechanical interlocking between the interface surfaces through the model geometry constructed using profilometer data measured from the test specimens. However, this representation of coating roughness and asperities is not sufficient to account for the measured increase in effective shear strength for high roughness coatings. The further addition of an ICH mechanism leads to accurate predictions of the experimental measurements. Increased compressive stresses in the coating material and increased compression in the interface are revealed to be the key mechanistic differences between smooth and rough coatings. While the geometric differences provide some increase in effective shear strength for rough coatings, a localised ICH mechanism is required to capture the entire experimental increase in strength.

The ICH mechanism is applied at the sub-micron size-scale of the micro-mechanical coating asperity model. However, ICH can be interpreted as a phenomenological representation of smaller nano-scale

30

mechanisms at the size-scale of coating-substrate interdigitation along the surface of asperities. Compressive stresses at nano-scale interdigitations will result in higher resistance to localised coating fracture, given the high strength of HA in compression.

Since such compressive regions are not computed for smooth coating-substrate interfaces, consequently the ICH mechanism is not activated. Our study suggests that the use of an ICH CZM formulation coupled with geometrically represented surface roughness is sufficient to capture the increase in interface strength due to surface roughness.

Micro-scale simulations also reveal higher localised intra-coating stress concentrations for rough coating-substrate interfaces suggesting that coating damage may be more pronounced in rough interfaces near to large asperities. Such localised stress concentrations may exceed the coating compressive load resistance [64], resulting in localised damage within the coating material. This may explain the experimental finding that ~10% of coating remains on the substrate following lap-shear testing of rough interfaces, compared to only ~3% for smooth coating-substrate interfaces.

While the proposed compression hardening mechanism provides good agreement with the experimentally measured data in respect to an increased effective mode II strength for rough coating-substrate interfaces, it is recognised that additional mechanisms may be involved. For example, it is possible that the chemical structure of the CaP/AZ31 might not be identical for the three coating/roughness interfaces. As the sets of three substrates of each type were prepared using the same SiC grit size paper and IPA rinsing protocol, such disparities are less likely. Alternatively, intermixing of film and AZ31substrate constituents could occur during the energetic sputter deposition process resulting in the stronger interface bond strength and increased shear strength observed. Such intermixing has been observed previously for magnetron sputtered CaP film on Ti alloy [69] and CaP on PEEK [70] substrates. Generally, intermixing occurs through two mechanisms, via direct ion implantation, unlikely for magnetron sputtering where the ion energies are relatively low (< 20 eV) or via sputtering and redeposition of the substrate atoms. Generally, substrate roughness is believed to influence the local sputter and redeposition rates and this has been studied by

31

comparing experimentally measured effective sputter rates for flat solid samples and more rough compressed powder disks [71,72]. It was found that both the effective sputter rate and the amount of redeposited material was larger for the compressed powder disks, i.e., the rougher surface. A numerical simulation of a rough surface morphology represented by a periodic structure [73] also shows that the sputtering yield increases with the feature size and hence with the surface roughness. In the present case, it is possible that, for the rougher substrates, increased sputtering and redeposition of Mg species may result in more efficient intermixing thereby increasing the shear load to failure conditions. However, further evidence for these effects is beyond the scope of the current study and will be addressed in subsequent work.

7   Conclusion

Double lap shear testing of CaP coated magnesium alloys has shown that there is a relationship between alloy roughness and shear strength. Rough substrates require the highest load to cause failure. Coating thickness does not exhibit the same trend, with no significant difference seen between 0.37, 0.83 and 1.34 µm coating thicknesses. Macro-scale finite element models of lap-shear tests allowed for calibration of effective interface shear strength as a function of coating thickness and coating roughness using a cohesive zone model of interface failure. Micro-scale finite element models were constructed using experimental profilometry measurements to gain insight into the relationship between coating roughness and effective shear strength. Such micro-scale analyses suggest that the presence of large asperities in rough coatings lead to localised regions of interface compression, which in turn result in localised shear hardening of the interface. This results in higher effective shear strengths for rough coatings, as observed experimentally.

32

University, the National University Ireland, Galway, North Carolina Agricultural and Technical State University, University of Pittsburgh, University of Cincinnati and Cincinnati Children's Hospital. The authors acknowledge access to computing facilities provided by the Irish Centre for High-End Computing (ICHEC).

Declaration of Interest

Declaration of interest – None.

References

[1]   M.S. Uddin, C. Hall, P. Murphy, Surface treatments for controlling corrosion rate of biodegradable Mg and Mg-based alloy implants, Sci. Technol. Adv. Mater. 16 (2015) 53501. doi:10.1088/1468-6996/16/5/053501.

[2]   V.J. Mailoo, V. Srinivas, J. Turner, W.D. Fraser, Beware of bone pain with bisphosphonates, BMJ Case Rep. 12 (2019) e225385. doi:10.1136/bcr-2018-225385.

[3]   Y. Yang, C. He, Dianyu E, W. Yang, F. Qi, D. Xie, L. Shen, S. Peng, C. Shuai, Mg bone implant: Features, developments and perspectives, Mater. Des. 185 (2020). doi:10.1016/j.matdes.2019.108259.

[4]   E. Pérez-Pevida, A. Brizuela-Velasco, D. Chávarri-Prado, A. Jiménez-Garrudo, F. Sánchez-Lasheras, E. Solaberrieta-Méndez, M. Diéguez-Pereira, F.J. Fernández-González, B. Dehesa-Ibarra, F. Monticelli, Biomechanical Consequences of the Elastic Properties of Dental Implant Alloys on the Supporting Bone: Finite Element Analysis., Biomed Res. Int. 2016 (2016) 1850401. doi:10.1155/2016/1850401.

[5]   L. Liu, K. Gebresellasie, B. Collins, H. Zhang, Z. Xu, J. Sankar, Y.C. Lee, Y. Yun, Degradation rates of pure zinc, magnesium, and magnesium alloys measured by volume loss, mass loss, and hydrogen evolution, Appl. Sci. 8 (2018). doi:10.3390/app8091459.

[6]   M. Kuhlefelt, P. Laine, L. Suominen-Taipale, T. Ingman, C. Lindqvist, H. Thorén, Risk factors contributing to symptomatic miniplate removal: a retrospective study of 153 bilateral sagittal split osteotomy patients, Int. J. Oral Maxillofac. Surg. 39 (2010) 430–435. doi:10.1016/j.ijom.2010.01.016.

[7]   P. Schumann, D. Lindhorst, M.E.H. Wagner, A. Schramm, N.-C. Gellrich, M. Rucker, Perspectives on resorbable osteosynthesis materials in craniomaxillofacial surgery., Pathobiology. 80 (2013) 211–217. doi:10.1159/000348328.

[8]   G. Reith, V. Schmitz-Greven, K.O. Hensel, M.M. Schneider, T. Tinschmann, B. Bouillon, C. Probst, Metal implant removal: benefits and drawbacks – a patient survey, BMC Surg. 15 (2015) 96. doi:10.1186/s12893-015-0081-6.

[9]   S. Pina, J.M.F. Ferreira, Bioresorbable plates and screws for clinical applications: A review, J. Healthc. Eng. 3 (2012) 243–260. doi:10.1260/2040-2295.3.2.243.

[10]   H. Waizy, J.-M. Seitz, J. Reifenrath, A. Weizbauer, F.-W. Bach, A. Meyer-Lindenberg, B. Denkena, H. Windhagen, Biodegradable magnesium implants for orthopedic applications, J. Mater. Sci. 48 (2013). doi:10.1007/s10853-012-6572-2.

[11]   Y. Ding, C. Wen, P. Hodgson, Y. Li, Effects of alloying elements on the corrosion behavior and biocompatibility of biodegradable magnesium alloys: A review, J. Mater. Chem. B. 2 (2014) 1912–1933. doi:10.1039/c3tb21746a.

[12]   S. Agarwal, J. Curtin, B. Duffy, S. Jaiswal, Biodegradable magnesium alloys for orthopaedic applications: A review on corrosion, biocompatibility and surface modifications, Mater. Sci. Eng. C. 68 (2016) 948–963. doi:10.1016/j.msec.2016.06.020.

[13]   B. Ratna Sunil, C. Ganapathy, T.S. Sampath Kumar, U. Chakkingal, Processing and mechanical behavior of lamellar structured degradable magnesium-hydroxyapatite implants, J. Mech. Behav. Biomed. Mater. (2014). doi:10.1016/j.jmbbm.2014.08.016.

[14] E. Moradi, M. Ebrahimian-Hosseinabadi, M. Khodaei, S. Toghyani, Magnesium/nano-hydroxyapatite porous biodegradable composite for biomedical applications, Mater. Res. Express. 6 (2019) 075408. doi:10.1088/2053-1591/ab187f.

[15] E.C. Huse, A new ligature, Chicago Med J Exam. 172 (1878) 11.

[16] F. Witte, The history of biodegradable magnesium implants: A review☆, Acta Biomater. 6 (2010). doi:10.1016/j.actbio.2010.02.028.

[17] F. Witte, N. Hort, C. Vogt, S. Cohen, K.U. Kainer, R. Willumeit, F. Feyerabend, Degradable biomaterials based on magnesium corrosion, Curr. Opin. Solid State Mater. Sci. 12 (2008) 63–72. doi:10.1016/j.cossms.2009.04.001.

[18] Y.F. Zheng, X.N. Gu, F. Witte, Biodegradable metals, Mater. Sci. Eng. R Reports. 77 (2014) 1–34. doi:10.1016/j.mser.2014.01.001.

[19] L.C. Campanelli, U.F.H. Suhuddin, A.Í.S. Antonialli, J.F. Dos Santos, N.G. De Alcântara, C. Bolfarini, Metallurgy and mechanical performance of AZ31 magnesium alloy friction spot welds, J. Mater. Process. Technol. (2013). doi:10.1016/j.jmatprotec.2012.11.002.

[20] A.R. Boyd, C. O'Kane, B.J. Meenan, Control of calcium phosphate thin film stoichiometry using multi-target sputter deposition, Surf. Coatings Technol. 233 (2013) 131–139. doi:https://doi.org/10.1016/j.surfcoat.2013.04.017.

[21] J.G. Acheson, S. McKillop, P. Lemoine, A.R. Boyd, B.J. Meenan, Control of magnesium alloy corrosion by bioactive calcium phosphate coating: Implications for resorbable orthopaedic implants, Materialia. 6 (2019) 10. doi:10.1016/j.mtla.2019.100291.

[22] R. Surmenev, Radio Frequency Magnetron Sputter Deposition as a Tool for Surface Modification of Medical Implants, in: A. Vladescu (Ed.), IntechOpen, Rijeka, 2017: p. Ch. 12. doi:10.5772/66396.

[23] E. Brooks, M. Ehrensberger, Bio-Corrosion of Magnesium Alloys for Orthopaedic Applications, J. Funct. Biomater. 8 (2017) 38. doi:10.3390/jfb8030038.

[24] P.C. Banerjee, S. Al-Saadi, L. Choudhary, S.E. Harandi, R. Singh, Magnesium implants: Prospects and challenges, Materials (Basel). 12 (2019) 1–21. doi:10.3390/ma12010136.

[25] R.A. Surmenev, M.A. Surmeneva, I.Y. Grubova, R. V. Chernozem, B. Krause, T. Baumbach, K. Loza, M. Epple, RF magnetron sputtering of a hydroxyapatite target: A comparison study on polytetrafluorethylene and titanium substrates, Appl. Surf. Sci. 414 (2017) 335–344. doi:10.1016/j.apsusc.2017.04.090.

[26] T.K. Monsees, F.A. Azem, C.M. Cotrut, M. Braic, R. Abdulgader, I. Pana, I. Birlik, A. Kiss, R. Booysen, A. Vladescu, Biodegradable ceramics consisting of hydroxyapatite for orthopaedic implants, Coatings. 7 (2017). doi:10.3390/coatings7110184.

[27] A.I. Kozelskaya, S.E. Kulkova, A.Y. Fedotkin, E.N. Bolbasov, Y.M. Zhukov, L. Stipniece, A. V. Bakulin, A.S. Useinov, E. V. Shesterikov, J. Locs, S.I. Tverdokhlebov, Radio frequency magnetron sputtering of Sr- and Mg-substituted β-tricalcium phosphate: Analysis of the physicochemical properties and deposition rate of coatings, Appl. Surf. Sci. (2020). doi:10.1016/j.apsusc.2019.144763.

[28] A.M. Aronov, V.F. Pichugin, E. V. Eshenko, M.A. Ryabtseva, R.A. Surmenev, S.I. Tverdokhlebov, E. V. Shesterikov, Thin calcium-phosphate coatings produced by RF magnetron sputtering and prospects for their use in biomedical engineering, Biomed. Eng. (NY). 42 (2008) 123–127. doi:10.1007/s10527-008-9029-9.

[29] V.F. Pichugin, R.A. Surmenev, E.V. Shesterikov, M.A. Ryabtseva, E.V. Eshenko, S.I. Tverdokhlebov, O. Prymak, M. Epple, The preparation of calcium phosphate coatings on titanium and nickel–titanium by rf-magnetron-sputtered deposition: Composition, structure and micromechanical properties, Surf. Coatings Technol. 202 (2008) 3913–3920. doi:10.1016/j.surfcoat.2008.01.038.

[30] P. Cheang, K.A. Khor, Addressing processing problems associated with plasma spraying of hydroxyapatite coatings, Biomaterials. 17 (1996) 537–544. doi:10.1016/0142-9612(96)82729-3.

[31] J.W.M. Heemskerk, E.M. Bevers, T. Lindhout, Platelet activation and blood coagulation., Thromb. Haemost. 88 (2002) 186–193.

[32] K. Ishikawa, A. Kareiva, Sol–gel synthesis of calcium phosphate-based coatings – A review, Chemija. 31 (2020). doi:10.6001/chemija.v31i1.4169.

[33] M. Qadir, Y. Li, C. Wen, Ion-substituted calcium phosphate coatings by physical vapor deposition magnetron sputtering for biomedical applications: A review, Acta Biomater. (2019). doi:10.1016/j.actbio.2019.03.006.

[34] A.R. Boyd, B.J. Meenan, N.S. Leyland, Surface characterisation of the evolving nature of radio frequency (RF) magnetron sputter deposited calcium phosphate thin films after exposure to physiological solution, Surf. Coatings Technol. 200 (2006) 6002–6013. doi:10.1016/j.surfcoat.2005.09.032.

[35] A.R. Boyd, L. Rutledge, L.D. Randolph, B.J. Meenan, Strontium-substituted hydroxyapatite coatings deposited via a co-deposition sputter technique, Mater. Sci. Eng. C. 46 (2015) 290–300. doi:10.1016/j.msec.2014.10.046.

[36] D. Rohanová, D. Horkavcová, A. Helebrant, A.R. Boccaccini, Assessment of in vitro testing approaches for bioactive inorganic materials, J. Non. Cryst. Solids. 432 (2016) 53–59. doi:10.1016/j.jnoncrysol.2015.03.016.

[37] T.M. Mukhametkaliyev, M.A. Surmeneva, A. Vladescu, C.M. Cotrut, M. Braic, M. Dinu, M.D. Vranceanu, I. Pana, M. Mueller, R.A. Surmenev, A biodegradable AZ91 magnesium alloy coated with a thin nanostructured hydroxyapatite for improving the corrosion resistance, Mater. Sci. Eng. C. 75 (2017) 95–103. doi:10.1016/j.msec.2017.02.033.

[38] H. Hu, X. Nie, Y. Ma, Corrosion and Surface Treatment of Magnesium Alloys, in: Magnes. Alloy. - Prop. Solid Liq. States, InTech, 2014. doi:10.5772/58929.

[39] R.A. Surmenev, M.A. Surmeneva, A critical review of decades of research on calcium phosphate–based coatings: How far are we from their widespread clinical application?, Curr. Opin. Biomed. Eng. 10 (2019) 35–44. doi:10.1016/j.cobme.2019.02.003.

[40] T.W. Bauer, Hydroxyapatite: coating controversies., Orthopedics. 18 (1995) 885–8.

[41] A. Mumith, V.S. Cheong, P. Fromme, M.J. Coathup, G.W. Blunn, The effect of strontium and silicon substituted hydroxyapatite electrochemical coatings on bone ingrowth and osseointegration of selective laser sintered porous metal implants, PLoS One. 15 (2020) e0227232. doi:10.1371/journal.pone.0227232.

[42] K. Søballe, S. Overgaard, The current status of hydroxyapatite coating of prostheses, J. Bone Joint Surg. Br. 78-B (1996) 689–691. doi:10.1302/0301-620X.78B5.0780689.

[43] S. Overgaard, Calcium phosphate coatings for fixation of bone implants: Evaluated mechanically and histologically by stereological methods, Acta Orthop. Scand. 71 (2000) 1–74.

36

doi:10.1080/000164700753759574.

[44] J.G. Acheson, S. McKillop, J. Ward, A. Roy, Z. Xu, A.R. Boyd, P. Lemoine, P.N. Kumta, J. Sankar, B.J. Meenan, Effects of strontium-substitution in sputter deposited calcium phosphate coatings on the rate of corrosion of magnesium alloys, Surf. Coatings Technol. 421 (2021) 127446. doi:https://doi.org/10.1016/j.surfcoat.2021.127446.

[45] M. Qadir, Y. Li, C. Wen, Ion-substituted calcium phosphate coatings by physical vapor deposition magnetron sputtering for biomedical applications: A review, Acta Biomater. 89 (2019) 14–32. doi:10.1016/j.actbio.2019.03.006.

[46] K. Chen, J. Dai, X. Zhang, Improvement of corrosion resistance of magnesium alloys for biomedical applications, Corros. Rev. 33 (2015) 101–117. doi:10.1515/corrrev-2015-0007.

[47] B. FitzGibbon, P. McGarry, Development of a test method to investigate mode II fracture and dissection of arteries, Acta Biomater. 121 (2021) 444–460. doi:10.1016/j.actbio.2020.11.023.

[48] J.P. McGarry, É. Ó Máirtín, G. Parry, G.E. Beltz, Potential-based and non-potential-based cohesive zone formulations under mixed-mode separation and over-closure. Part I: Theoretical analysis, J. Mech. Phys. Solids. 63 (2014) 336–362. doi:10.1016/j.jmps.2013.08.020.

[49] G.I. Barenblatt, The formation of equilibrium cracks during brittle fracture. General ideas and hypotheses. Axially-symmetric cracks, J. Appl. Math. Mech. 23 (1959) 622–636. doi:10.1016/0021-8928(59)90157-1.

[50] X.-P. Xu, A. Needleman, A.R. J, B.G. and R.J. R, F.J. and S.J.R. Bozzolo G, N.A. and S.S. Christman T, F.J. and S.J. R, H.K. S, H.R. and R.J. R, L.E. H, L.A. and P.J. M, K.A.D.N.S.R.A.D.L. and S.D.M. Marieb T N, A.R.J. and S.C.F. McHugh P E, V.A.G.A.R.J. and S.C.F. McHugh P E, N. A, N. A, N. A, N. A, N.A. and R.J. R, S.S. and T. V Needleman A, N.A. and T. V, L.P. and B.P.F. Nutt S R, N.S.R. and N. A, A.R.J. and N.A. Peirce D, S.C.F. and N.A. Peirce D, N.A. and N.S.R. Povirk G, R.J. R, R.J. R, R.J. R, F.J. and S.J.R. Rose J H, S.J.R. and F.J. Rose J H, N.A. and T. V Sørensen N, S.C.F. and V.A.G. Suo Z, T. V, T. V, Void nucleation by inclusion debonding in a crystal matrix, Model. Simul. Mater. Sci. Eng. 1 (1993) 111–132. doi:10.1088/0965-0393/1/2/001.

[51] M.J. van den Bosch, P.J.G. Schreurs, M.G.D. Geers, An improved description of the exponential Xu and Needleman cohesive zone law for mixed-mode decohesion, Eng. Fract. Mech. 73 (2006) 1220–1234. doi:10.1016/j.engfracmech.2005.12.006.

[52] É.Ó. Máirtín, G. Parry, G.E. Beltz, J.P. McGarry, Potential-based and non-potential-based cohesive zone formulations under mixed-mode separation and over-closure–Part II: Finite element applications, J. Mech. Phys. Solids. 63 (2014) 363–385. doi:10.1016/J.JMPS.2013.08.019.

[53] C.G. Hopkins, P.E. McHugh, J.P. McGarry, Computational investigation of the delamination of polymer coatings during stent deployment, Ann. Biomed. Eng. 38 (2010) 2263–2273. doi:10.1007/s10439-010-9972-y.

[54] E.A. Gallagher, S. Lamorinière, P. McGarry, Multi-axial damage and failure of medical grade carbon fibre reinforced PEEK laminates: Experimental testing and computational modelling, J. Mech. Behav. Biomed. Mater. 82 (2018) 154–167. doi:10.1016/j.jmbbm.2018.03.015.

[55] E.A. Gallagher, S. Lamorinière, P. McGarry, Finite element investigation into the use of carbon fibre reinforced PEEK laminated composites for distal radius fracture fixation implants, Med. Eng. Phys. 67 (2019) 22–32. doi:10.1016/j.medengphy.2019.03.006.

[56] J.P. McGarry, P.E. McHugh, Modelling of in vitro chondrocyte detachment, J. Mech. Phys. Solids. 56 (2008) 1554–1565. doi:10.1016/j.jmps.2007.08.001.

[57] A.R. Boyd, L. Rutledge, L.D. Randolph, I. Mutreja, B.J. Meenan, The deposition of strontium-substituted hydroxyapatite coatings, J. Mater. Sci. Mater. Med. 26 (2015) 1–14. doi:10.1007/s10856-014-5377-z.

[58] L. Stipniece, S. Wilson, J.M. Curran, R. Chen, K. Salma-Ancane, P.K. Sharma, B.J. Meenan, A.R. Boyd, Strontium substituted hydroxyapatite promotes direct primary human osteoblast maturation, Ceram. Int. (2020). doi:10.1016/j.ceramint.2020.09.182.

[59] L. Robinson, K. Salma-Ancane, L. Stipniece, B.J. Meenan, A.R. Boyd, The deposition of strontium and zinc Co-substituted hydroxyapatite coatings, J. Mater. Sci. Mater. Med. 28 (2017). doi:10.1007/s10856-017-5846-2.

[60] W.S. Rasband, ImageJ, U. S. Natl. Institutes Heal. Bethesda, Maryland, USA. (2017).

[61] S. Preibisch, S. Saalfeld, P. Tomancak, Globally optimal stitching of tiled 3D microscopic image acquisitions, Bioinformatics. 25 (2009) 1463–1465. doi:10.1093/bioinformatics/btp184.

[62] G. V. Lubarsky, P. Lemoine, B.J. Meenan, S. Deb, I. Mutreja, P. Carolan, N. Petkov, Enamel proteins mitigate mechanical and structural degradations in mature human enamel during acid attack, Mater. Res. Express. 1 (2014) 025404. doi:10.1088/2053-1591/1/2/025404.

[63] T. Yokoyama, Experimental determination of impact tensile properties of adhesive butt joints with the split Hopkinson bar, J. Strain Anal. Eng. Des. (2003). doi:10.1243/030932403765310563.

[64] M. Prakasam, J. Locs, K. Salma-Ancane, D. Loca, A. Largeteau, L. Berzina-Cimdina, Fabrication, Properties and Applications of Dense Hydroxyapatite: A Review, J. Funct. Biomater. 6 (2015) 1099–1140. doi:10.3390/jfb6041099.

[65] M. Razavi, M. Fathi, O. Savabi, S. Mohammad Razavi, B. Hashemi Beni, D. Vashaee, L. Tayebi, Controlling the degradation rate of bioactive magnesium implants by electrophoretic deposition of akermanite coating, Ceram. Int. 40 (2014) 3865–3872. doi:10.1016/j.ceramint.2013.08.027.

[66] S. Budhe, A. Ghumatkar, N. Birajdar, M.D. Banea, Effect of surface roughness using different adherend materials on the adhesive bond strength, Appl. Adhes. Sci. 3 (2015) 20. doi:10.1186/s40563-015-0050-4.

[67] J. Zhang, X. Zhao, Y. Zuo, Z. J, X. Zhang, Effect of Surface Pretreatment on Adhesive Properties of Aluminum Alloys, 材料科学与技术. 24 (2008) 236–240.

[68] E.M. Feerick, J. Kennedy, H. Mullett, D. FitzPatrick, P. McGarry, Investigation of metallic and carbon fibre PEEK fracture fixation devices for three-part proximal humeral fractures, Med. Eng. Phys. 35 (2013) 712–722. doi:10.1016/j.medengphy.2012.07.016.

[69] Y.T. Zhao, Z. Zhang, Q.X. Dai, D.Y. Lin, S.M. Li, Microstructure and bond strength of HA(+ZrO2+Y2O3)/Ti6Al4V composite coatings fabricated by RF magnetron sputtering, Surf. Coatings Technol. 200 (2006) 5354–5363. doi:10.1016/j.surfcoat.2005.06.010.

[70] S. Hussain, L. Rutledge, J.G. Acheson, A.R. Boyd, B.J. Meenan, The surface characterisation of polyetheretherketone (Peek) modified via the direct sputter deposition of calcium phosphate thin films, Coatings. 10 (2020) 1–26. doi:10.3390/coatings10111088.

[71] F. Boydens, W.P. Leroy, R. Persoons, D. Depla, The influence of target surface morphology on the deposition flux during direct-current magnetron sputtering, Thin Solid Films. 531 (2013) 32–41. doi:10.1016/j.tsf.2012.11.097.

[72] D. Depla, On the effective sputter yield during magnetron sputter deposition, Nucl. Instruments

Methods Phys. Res. Sect. B Beam Interact. with Mater. Atoms. 328 (2014) 65–69. doi:10.1016/j.nimb.2014.03.001.

[73]   I. Bizyukov, A. Mutzke, R. Schneider, Effect of increasing surface roughness on sputtering and reflection, Probl. At. Sci. Technol. (2012) 111–113.